A Spacer Cation Assisted Nucleation and Growth Strategy Enables Efficient and High-Luminance Quasi-2D Perovskite LEDs

Lingmei Kong, Yaning Luo, Lyudmila Turyanska,* Ting Zhang, Zhipeng Zhang, Guichuan Xing, Yingguo Yang, Chengxi Zhang,* and Xuyong Yang*

Quasi-2D Ruddlesden-Popper perovskites receive tremendous attention for application in light-emitting diodes (LEDs). However, the role of organic ammonium spacers on perovskite film has not been fully-understood. Herein, a spacer cation assisted perovskite nucleation and growth strategy, where guanidinium (GA$^+$) spacer is introduced into the perovskite precursor and at the interface between the hole transport layer (HTL) and the perovskite, to achieve dense and uniform perovskite films with enhanced optical and electrical performance is developed. A thin GABr interface pre-formed on HTL provides more nucleation sites for perovskite crystal; while the added GA$^+$ in perovskite reduces the crystallization rate due to strong hydrogen bonding interacts with intermediates, which promotes the growth of enhanced-quality quasi-2D perovskite films. The ionized ammonium group ($-NH_3^+$) of GA$^+$ also favors formation of polydisperse domain distribution, and amine or imine ($-NH_2$ or $=NH$) group interact with perovskite defects through coordination bonding. The spacer cation assisted nucleation and growth strategy is advantageous for producing efficient and high-luminance perovskite LEDs, with a peak external quantum efficiency of over 20% and a luminance up to 100 000 cd m^{-2}. This work can inform and underpin future development of high-performance perovskite LEDs with concurrent high efficiency and brightness.

1. Introduction

Metal halide perovskites have gained tremendous attention for applications in light-emitting diodes (LEDs),[1–8] due to their distinctive optical and electrical properties.[9–11] Of particular interest are quasi-2D perovskites, which have high exciton binding energy (hundreds of meV), increased ion migration activation energy,[12] and more resistant to moisture than their 3D counterparts,[13,14] which is beneficial for high-performance and stable LEDs.[15,16] Quasi-2D Ruddlesden-Popper perovskites have the general formula of $L_2A_{n-1}B_nX_{3n+1}$, where L is large organic ammonium such as butyl-ammonium (BA) as spacer, A is a monovalent cation (Cs/methylammonium/formamidinium), B is a divalent metal cation such as Pb, X is a halide anion (Cl/Br/I), and n is the number of inorganic BX_6^{4-} octahedral sheets between two spacer layers.[17,18]

It has been found that organic ammonium cations play a key role in crystallization kinetics of perovskites because of the ability to form weak hydrogen bonds with perovskite intermediate during crystallization process. Quasi-2D perovskite can form different domain distributions (different n) due to thermodynamic mixing and variable formation energy of the domains, that can be tunable by ammonium cations.[19,20] Consequently, both the resulting film morphology and domain distribution in quasi-2D perovskite are strongly related to organic ammonium cations. With respect to film quality, a dense and uniform perovskite film with low defects density

L. Kong, Y. Luo, T. Zhang, C. Zhang, X. Yang
Key Laboratory of Advanced Display and System Applications of, Ministry of Education
Shanghai University
149 Yanchang Road, Shanghai 200072, China
E-mail: Andrew_xiwa@shu.edu.cn; Yangxy@shu.edu.cn

The ORCID identification number(s) for the author(s) of this article can be found under https://doi.org/10.1002/adfm.202209186.

L. Turyanska
Faculty of Engineering
University of Nottingham
Nottingham NG7 2RD, UK
E-mail: Lyudmila.Turyanska@nottingham.ac.uk

Z. Zhang, G. Xing
Institute of Applied Physics and Materials Engineering
University of Macau
Macau SAR 999078, China

Y. Yang
Shanghai Synchrotron Radiation Facility (SSRF), Zhangjiang Lab
Shanghai Advanced Research Institute
Chinese Academy of Sciences
Shanghai 201204, China

**ADVANCED
SCIENCE NEWS**
www.advancedsciencenews.com

**ADVANCED
FUNCTIONAL
MATERIALS**
www.afm-journal.de

is required to improve the performance of perovskite LEDs. Comparing to the approaches reported to date, such as solvent engineering, modification of underlaying layer and nanocrystal pinning,[19,21,22] the modulation of organic ammonium cations can offer additional advantage to improve charge transport.

The domain distribution affects the electrical and optical properties of the perovskite film. The fast energy transfer process between domains with different n values can result in carrier localization and accumulation in higher-n domains, which can in turn enhance the luminescence of the emitter. Lower-n domains confer higher stability but with lower efficiencies, presenting a compromise between enhanced device lifetime and electroluminescence (EL) performance.[16,23,24] Although quasi-2D perovskites have been widely adopted to produce high-performance LED, the role of organic ammonium spacers on perovskite film has not been fully recognized and utilized, especially its potential benefital effects on film morphology and charge transport.

In this work, we developed the GA+ spacer assisted nucleation and growth to regulate the nucleation and crystallization dynamics of quasi-2D perovskite films, achieving dense and uniform perovskite films with excellent optical and electrical performance. A very thin layer of GA+ is pre-deposited at the interface to serve as "seed" offering abundant nucleation sites for perovskite crystal, and the added GA+ with a short chain in the perovskite precursors leads to slower crystal growth rate due to the strong hydrogen bonding with perovskite intermediates, which facilitate the growth of high-quality perovskite. It is found that the GA+ in perovskite not only favors polydisperse domain distribution due to their ionized ammonium group, but also provide its lone pair electrons of amine or imine ($-NH_2$ or

$=NH$) group to coordinate uncoordinated lead defects, hence reducing the density of charge traps. By exploiting the beneficial effects of GA+ cation via a spacer assisted nucleation and growth strategy, we demonstrate an efficient and bright $BA_2Cs_{n-1}Pb_nBr_{3n+1}$ perovskite LED with enhanced overall operational parameters.

2. Results and Discussion

GA+ cation has nitrogen (N) atoms in two differently charged environments (Figure S1, Supporting Information), which are ionized ammonium group ($-NH_3^+$) and unsaturated N atoms in the amine or imine group ($-NH_2$ or $=NH$).[25] We propose that GA+ could facilitate the formation of hydrogen bonding to modulate the crystallization kinetics of perovskites and acts as a promoter for homogenous nucleation leading to the formation of perovskite films with continuous coverage and uniform grain sizes as well as enhanced optical properties.

The nitrogen-containing groups of GA+ form six hydrogen bonds with $[PbBr_6]^{4-}$ octahedron,[26] demonstrating a stronger hydrogen bonding capability of GA+ compared to commonly used BA+ ions. To explore the role of GA+ on quasi-2D $BA_2Cs_{n-1}Pb_nBr_{3n+1}$ perovskites, a set of samples was prepared with different GABr contents (molar ratio of 0, 0.1, 0.2, and 0.3 replacing BABr, named as GA-0, GA-0.1, GA-0.2, and GA-0.3). Film morphology investigations by scanning electron microscopic (SEM) measurements, revealed that the formed perovskite film without GA+ has a large number of pinholes, grain boundary gaps and inhomogeneous grain size ranging from ≈50 to ≈350 nm (**Figure 1**a,b). An improved film morphology is
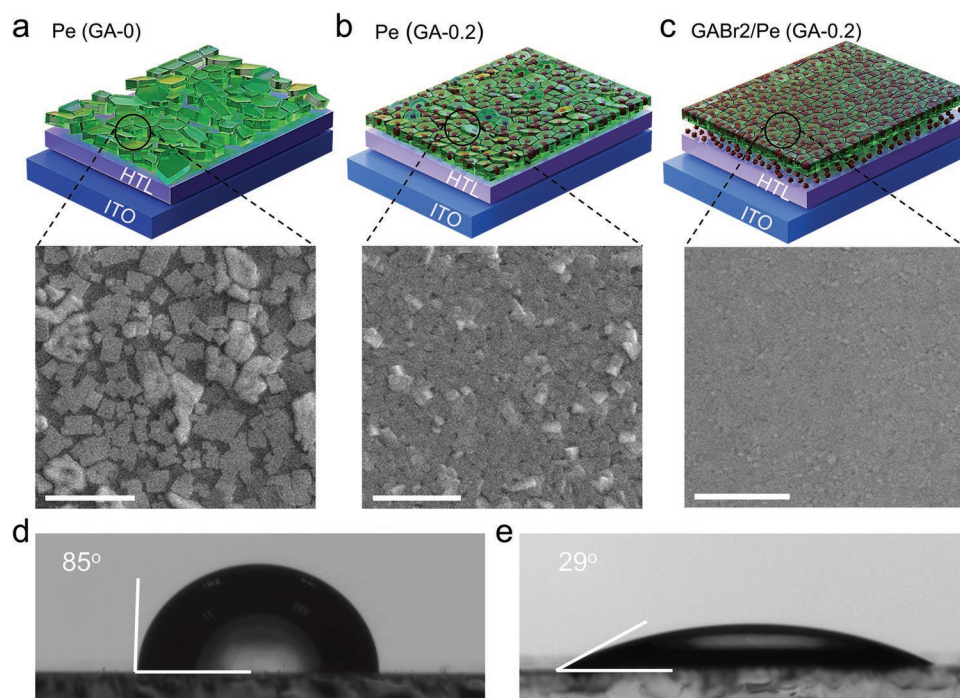

Figure 1. Schematic diagrams and corresponding top-view SEM images of the perovskite films produced a) without additive, Pe (GA-0) b) with GABr doping, Pe (GA-0.2); c) with interface layer, GABr2/Pe (GA-0.2). The scale bars are 500 nm. Contact angles of perovskite precursor droplets on d) HTL and e) HTL/GABr substrates.
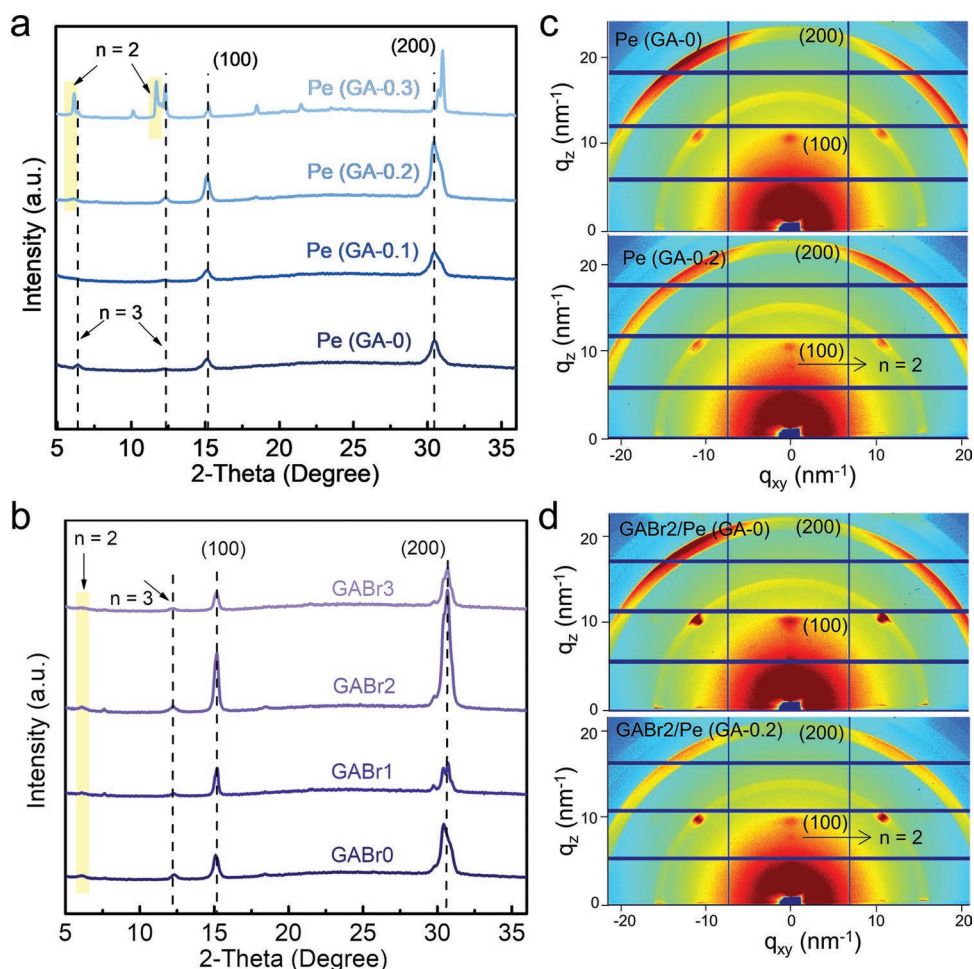
2209186 (2 of 8)

**ADVANCED
SCIENCE NEWS**

www.advancedsciencenews.com

**ADVANCED
FUNCTIONAL
MATERIALS**

www.afm-journal.de

Figure 2. XRD patterns of a) perovskite films treated with various GA+ concentrations in precursor solution and b) the Pe (GA-0.2) films deposited on GABr interface. c) GIWAXS patterns of Pe (GA-0), Pe (GA-0.2), and d) GABr2/Pe (GA-0) and GABr2/Pe (GA-0.2).

also confirmed by the Atomic Force Microscopy (AFM) studies, where the root mean square (r.m.s) roughness of 2.37 nm is measured for GABr2/Pe (GA-0.2) film compared to (8.44 nm) for the Pe (GA-0) film.

The large-size grains are known to lead to exciton dissociation due to the weaker exciton binding energy.[27] In contrast, continuous films formed in the presence of GA+ (0.2) have a noticeable improvement of grain size uniformity (Figure S2, Supporting Information). The strong hydrogen bonding of GA+ with perovskite intermediates leads to slower crystal growth,[28] which facilitates the formation of high-quality perovskite crystals. However, further increase of GA+-content causes poor crystallinity and the appearance of heterogeneous phases is detected in the X-ray diffraction (XRD) patterns (**Figure 2**a), which is consistent with the previous reports.[29,30]

The GA+ is also considered to increase nucleation sites of perovskite crystals, which is of equal importance to induce high-quality perovskite crystal growth. We pre-deposited a thin layer (< 3 nm) of GABr on the hole transport layer (HTL) below the perovskite layer, and the morphological studies of the Pe (GA-0.2) on GABr2 (2 mg mL−1 GABr) modified HTL substrate revealed continuous and dense film with small grain sizes ranging from 10 to 30 nm (Figure 1c). The HTL used here is a mixture of

poly(9,9-dioctylfluorenyl-2,7-diyl)-co-(4,4′-(N-(4-sec-butylphenyl) diphenylamine) (TFB) and poly(9-vinylcarbazole) (PVK),[16] which gives favorable bandgap alignment. We note, that compared with commonly used poly (3,4-ethylenedioxythiophene): poly-(styrenesulfonate) (PEDOT:PSS), our perovskite film shows more stable PL intensity on TFB:PVK HTL (Figure S3, Supporting Information). However, PVK:TFB layer has a hydrophobic surface, which is not conducive to the growth of continuous coverage perovskite film (contact angle: 85º) because heterogeneous nucleation is inhibited for hydrophilic perovskite precursor. The modification of HTL with GABr leads to a gradual decrease of the contact angle with increasing GABr concentration from 1 to 3 mg mL−1, indicating that the hydrophilic nitrogen-containing groups of the GABr improve the surface wettability (Figure 1d,e). GABr concentration of 2 mg mL−1 is selected as optimal treatment for the following studies. Further increas of the GABr concentration (3 mg mL−1) results in a discontinuous film morphology, likely due to the disordered packing of crystals caused by the excessive number of nucleation sites (Figure S4, Supporting Information).

The large size of GA+ prevents it from occupying the cage surrounded by the [PbBr6]4− octahedra, which is linked to impeded periodic growth of perovskite.[31,32] XRD measurements

**ADVANCED
SCIENCE NEWS**

www.advancedsciencenews.com

**ADVANCED
FUNCTIONAL
MATERIALS**

www.afm-journal.de

were used to examine the effect of GA+ on crystal structure (Figure 2a). For the control sample (Pe (GA-0)), the diffraction peaks observed at 15.2° and 30.4° are attributed to characteristic (100) and (200) planes of CsPbBr$_3$, respectively.[33] Interestingly, the low dimensional perovskites with $n = 3$ and $n = 2$ domains gradually appear as the GA+ content increases, suggesting that polydisperse domain distribution tends to be formed in GA+ dominated perovskite film, while the BA+ favors a monodisperse distribution. We envisage that this difference may be related to the different binding energy between the molecule and perovskite: the stronger hydrogen bonding with the perovskite octahedron facilitates the growth of polydisperse domains. The observed increase of the diffraction peaks intensity with increasing GA+ content suggests that GA+ promotes crystallization, as a result of reduced crystal growth rate due to hydrogen bonding interaction with perovskite intermediates.[30] We note that the characteristic peak for (200) plane shifts toward higher values with GA content increasing to 0.3, which reflects lattice contraction of the perovskite phase. We attribute this to the fact that a smaller-size GA+ cation prefers to occupy the position of a larger-size cation BA+ in the crystal structure.[32] The XRD patterns reveal a negligible effect of the pre-deposited GABr on the perovskite crystal structure, however a significantly enhanced crystallization intensity is recorded for the GABr2/Pe (GA-0.2) sample (Figure 2b).

Grazing-incidence wide-angle X-ray scattering (GIWAXS) measurements were conducted to examine how GA+ or interfacial GABr affects the crystal composition and orientation of resulting perovskites (Figure 2c). Both Pe (GA-0) and Pe (GA-0.2) films exhibit apparent Bragg spots and Debye–Scherrer rings with nonuniform intensities along (200) plane, indicating the preferential orientation. Notably, the Pe (GA-0.2) film shows an additional diffraction peak at a smaller q value that is attributed to $n = 2$ domain, consistent with the XRD results. These diffraction spots are primarily observed along the q_z axis, we thus conclude that the low-dimensional layered perovskites are aligned parallel to the substrate.[19,34] Although the parallel arrangement of the perovskites is not conducive to the charge transport in the vertical direction within the perovskite film, the use of short-chain GA+ cations shorten the van der Waals gap between the adjacent perovskite phases, hence improving the charge transport. Similar to the XRD results, an increase in diffraction intensities is observed for the perovskite films grown on GABr pre-deposited HTL, GABr2/Pe (GA-0) or GABr2/Pe (GA-0.2) (Figure 2d), compared to those on bare HTL, Pe (GA-0) or Pe (GA-0.2) (Figure 2c). This result provides further confirmation of the beneficial effect of GABr on the perovskite crystallization. The GA+ cations present within and beneath the perovskite film synergistically modulates the crystallization kinetics, which facilitates the growth of high-quality films.

Optical properties of perovskite films were investigated to explore their potential for device applications. The relative intensity of the absorption peaks of layered perovskites increases with GA+ content increasing from 0 to 0.3 (**Figure 3**a). A strong absorption peak at 449 nm is attributed to $n = 3$ domain, and the peak at 419 nm, corresponding to $n = 2$ domain, becomes distinct for the samples with GA+ content exceeding 0.2. These observations demonstrate that the higher GA+
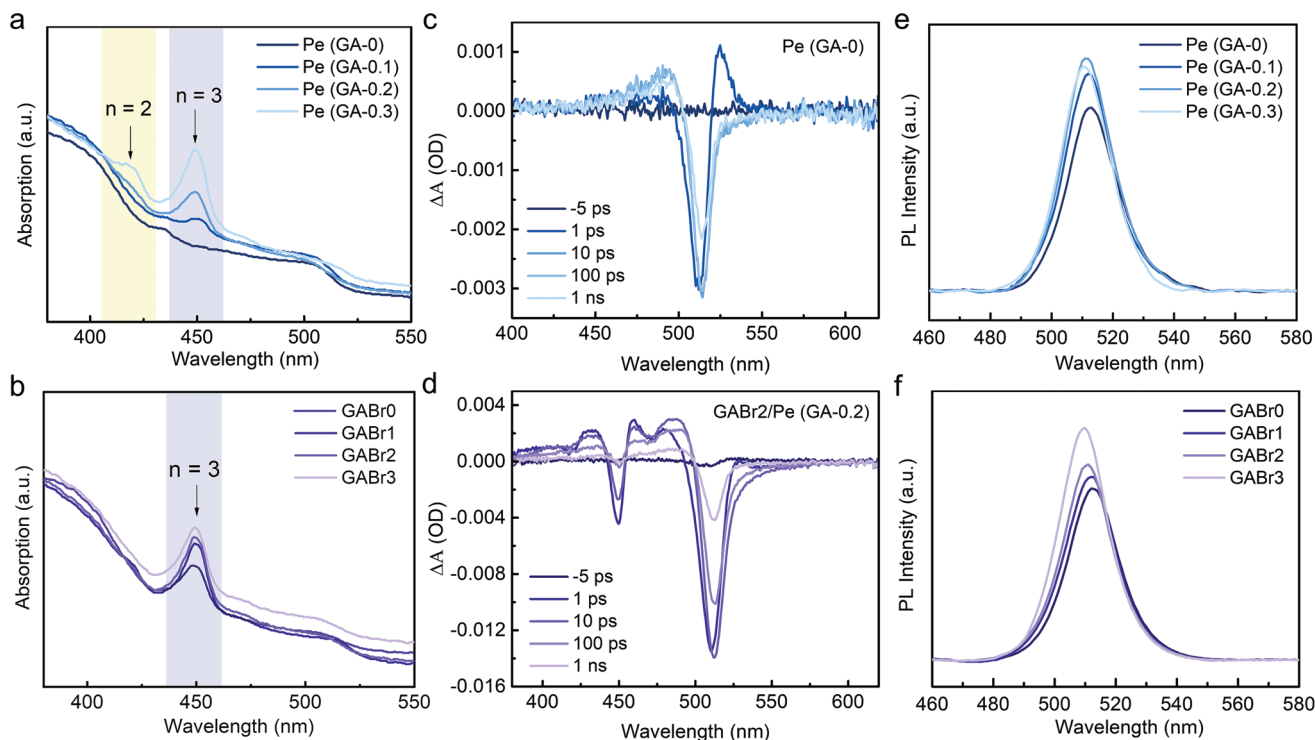

Figure 3. UV–visible spectra of a) perovskite films with various GA+ ratios and b) Pe (GA-0.2) films on HTL with different concentrations of GABr. TA spectra of c) Pe (GA-0) and d) GABr2/Pe (GA-0.2) films at selected timescales. Photoluminescence spectra of perovskite films produced with e) various GA+ ratios and f) different concentrations of GABr pre-deposited HTL.

2209186 (4 of 8)

content facilitates the growth of low-dimensional domains with $n \leq 3$. However, compared with GA^+ in perovskite films, GABr used as an interfacial layer pre-deposited onto HTL has a different effect on the perovskite domain distribution. The Pe (GA-0.2) films maintain $n = 3$ and high-dimensional domains with $n \geq 4$ (Figure 3b), with GABr content at the interface varying from 1 to 3 mg mL^{-1}. This indicates that the interfacial GA^+ does not participate in crystallization of low dimensional perovskites. Transient absorption (TA) spectroscopy was of the Pe (GA-0) film reveal pronounced ground-state bleaching (GSB) peaks within 1 ns, corresponding to high-dimensional domains with monodisperse domain distribution. For the GABr2/Pe (GA-0.2) films, the exciton resonances at $GSB_{n = 3}$ (peak at 449 nm) and $GSB_{n \geq 4}$ (peak at 512 nm) are initially observed, with only $GSB_{n \geq 4}$ remaining after a probe time of 100 ps due to exciton energy transfer from wide-bandgap domains to narrow-bandgap domains.[35,36] With the increase of GA^+ up to the ratio of < 0.3, the photoluminescence (PL) intensity of perovskite films is enhanced due to the decrease of the number of Pb^{2+} defects, which will be discussed in more details later. With further increase of the GA^+ ratio (≥ 0.3), the PL intensity decreases due to spatial and energy disorder caused by the excess of low-dimensional domains. The PL of samples on GABr pre-deposited HTL substrates is further improved, and a PL blueshift is observed with decreasing crystal size. The PL lifetime for Pe (GA-0), Pe (GA-0.2), and GABr2/Pe (GA-0.2) was determined to

be 76.9, 93.4, and 119.6 ns, respectively, indicating a lower defect density for GABr2/Pe (GA-0.2) film (Figure S5 and Table S1, Supporting Information). As a result, a high PL quantum yield (PLQY) of 87% was achieved for the GABr2/Pe (GA-0.2) film, which was significantly higher than that of Pe (GA-0) films (PLQY = 67%). We also note, that some beneficial effects of GABr treatment are observed with the surface-GABr modification, where an enhancement of the PL intensity and lifetime was observed due to a reduced defect density.

In order to investigate the interaction between GA^+ additive and perovskite, we further performed Fourier transform infrared (FTIR) spectroscopy (**Figure 4**a). The GA^+ characteristic peaks are observed at 1656, 1638, and 1540 cm^{-1} corresponding to C=N stretching vibration, NH_2 stretching vibration, and NH bending vibration, respectively.[37] All these peaks are shifted to higher frequencies in the Pe (GA-0.2) films. Notably, the formation of hydrogen bonding leads to a shift of the characteristic NH_2 and NH frequencies to lower values.[38] Thus, we concluded that the blueshift of NH_2 and NH is a result of the formation of both hydrogen bonding and coordination bonding, where NH_2 and NH provide their lone electron pairs to positively charged uncoordinated Pb^{2+} defects. The changes in domain distribution, as demonstrated above, confirm the effect of hydrogen bonding. X-ray photoelectron spectroscopy (XPS) was utilized to further investigate the possibility of coordination bonding (Figure 4b,c). XPS spectra reveal that the
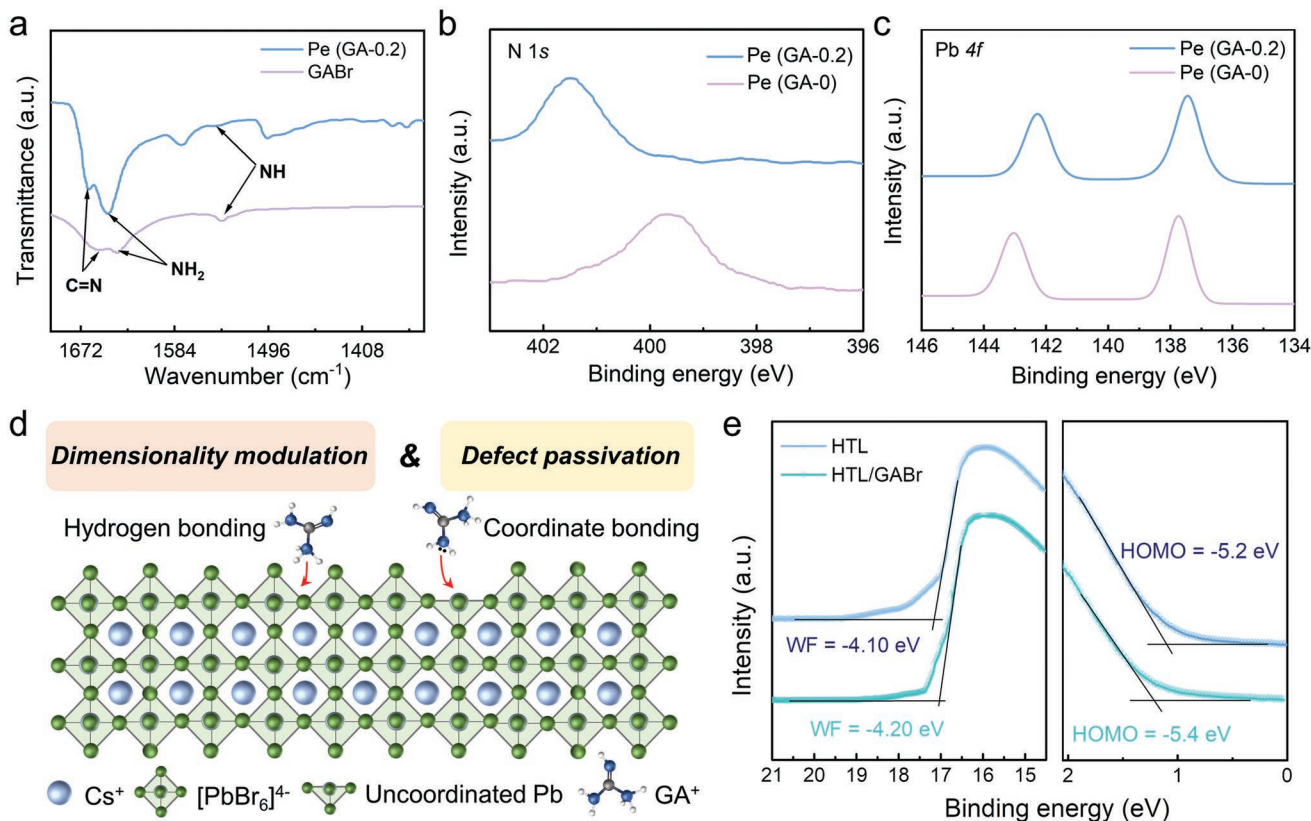

Figure 4. a) FTIR spectra of Pe (GA-0.2) and GABr. High-resolution XPS spectra of Pe (GA-0) and Pe (GA-0.2) for b) N 1s c) Pb 4f. d) The schematic mechanism of GA+ role on dimensionality modulation and defect passivation on CsPbBr3 perovskite. e) UPS spectra of high binding energy secondary-electron cutoffs and valence-band edge regions of HTL and HTL/GABr films.

N 1s resonance is shifted by 0.9 eV to higher binding energy with the incorporation of GA⁺, demonstrating a distinct change of electron cloud distribution of N atom compared to the control Pe (GA-0) sample. The photoemission spectra of Pb $4f$, revealed the shift of Pb $4f_{7/2}$ (137.7 eV) and Pb $4f_{5/2}$ (143.0 eV) signals toward lower binding energy, indicating the decrease of cationic charge of Pb^{2+} ions, which is caused by the formation of coordination bonding with N atoms (Figure 4d).[16,25] The $-NH_3^+$ groups contribute to dimensionality modulation by forming hydrogen bonding with $[PbBr_6]^{4-}$ octahedra, while $-NH_2$ or $=NH$ with lone pair electrons can coordinate with uncoordinated Pb^{2+} defects.

Ultraviolet photoelectron spectroscopy (UPS) was conducted to investigate the effect of interfacial GABr on the electronic structure of the HTL layer. Amine-containing conjugated small molecules are demonstrated to create interface dipoles that induce a vacuum-level shift and modify the work function (WF) of the conductor.[39] The WF of TFB:PVK HTL modified by GABr is 0.1 eV higher than that of TFB:PVK (Figure 4e). The HOMO energy levels are at −5.4 eV for TFB:PVK/GABr and −5.2 eV for TFB:PVK; the deeper HOMO state reduces the energy barrier between HTL and perovskite. The current density–voltage ($J–V$) characteristics of electron-only devices and hole-only devices (Figure S6, Supporting Information) allow us to conclude that electrons dominate injection in our devices, whereas the hole current is increased for GABr modified HTL, thus leading to a more balanced charge injection in the case of GABr2/Pe (GA-0.2) based LEDs. A better charge balance eliminates the accumulation of electrons at the edge of the emitting layer, which is conductive to decrease of the turn-on voltage of the device, enhancing device efficiency as well as suppressing efficiency roll-off.

Encouraged by the above findings, green emitting PeLEDs with a structure of ITO/TFB:PVK/GABr/Perovskite/TPBI/LiF/Al were fabricated (**Figure 5**a). The flat-band energy diagram of the PeLED (Figure 5b) has an improved charge balance due to deeper HOMO of the TFB:PVK after GABr modification. The PeLED performance characteristics are shown in Figure 5c–f and Figure S7 (Supporting Information). $J–V$ curves show that the current injection of Pe (GA-0.2)-based LEDs is more efficient than that of Pe (GA-0)-based LED, which is attributed to the decreased resistance of the perovskite film due to the incorporation of short-chain GA⁺ (Figure 5c). Although the current density is slightly reduced in the range of 3.5–7.5 V in the GABr2/Pe (GA-0.2)-based LEDs, an improved charge balance is indeed achieved. The LEDs with the GABr modifier showed a lower turn-on voltage V_{on} = 2 V, as well as a reduced leakage current due to the enhanced film morphology. At $V > V_{on}$, the radiative recombination is observed reaching the highest luminance of 105428 cd m⁻² for GABr2/Pe (GA-0.2)-based LEDs, which is approximately four times higher than that of the Pe (GA-0)-based LEDs (27228 cd m⁻²) (Figure 5d). The inset in Figure 5d shows bright green emission of the operating device at V = 3.5 V. Pe (GA-0), Pe (GA-0.2), and GABr2/Pe (GA-0.2)-based LEDs show the average external quantum efficiency (EQE) of 8.8%, 13.7%, 18.7%, respectively (Figure 5e). The EQE value presented here is an average measured for 20 devices, and the maximum EQE for GABr2/Pe (GA-0.2)-based LEDs is up to 20.1% (Figure 5f). The efficiency roll-off of the LED based on GABr2/Pe (GA-0.2) is enhanced due to improved charge balance, film quality, and interfacial contact.

Of particular importance is the observation of greatly improved half-lifetime in the GABr2/Pe (GA-0.2) with T_{50} = 15.3 h at an initial luminance of 100 cd m⁻², compared to 10.7 h for Pe (Ga-0.2) and 1.4 h for Pe (GA-0)-based LEDs (Figure S8, Supporting Information). The empirical acceleration factor is measured to be 1.55. The dramatic improvement in the operational stability by up to 11-times can be attributed to the introduction of GA⁺, which provide hydrogen bonds, thus making the lattice structure more stable. The overall performance of the PeLEDs represents one of the state-of-the-art device performances (see Table S2, Supporting Information), providing a convincing evidence of the effectiveness of our spacer cation assisted nucleation and growth strategy.
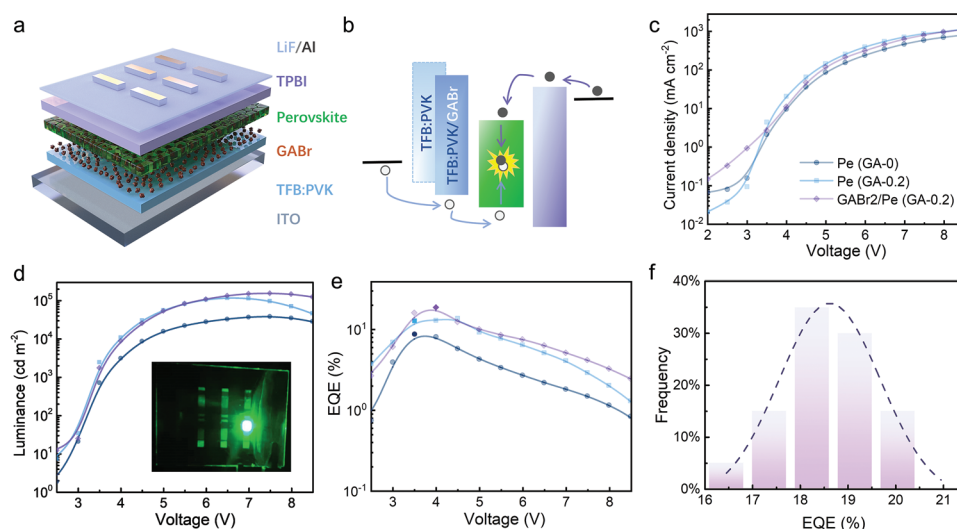

Figure 5. a) Schematics of the device structure, and b) corresponding flat-band energy diagram of perovskite LED. c) $J–V$, d) luminance–voltage ($L–V$), e) EQE–voltage (EQE–V) and f) Histogram statistical distribution of peak EQE for 20 devices. The inset in Figure 5d is a photo of the operating GABr2/Pe (GA-0.2) perovskite LEDs with an emitting area of 0.09 cm⁻².

3. Conclusion

Employing a GA$^+$ assisted nucleation and growth strategy, we successfully achieved high-performance green perovskite LEDs with external quantum efficiencies over 20% and luminance over 100 000 cd m^{-2}. The GA$^+$ cations preformed at the interface provide more nucleation sites for perovskite crystal, while GA$^+$ in perovskite show superior capability for crystallization control compared to BA$^+$ with single ammonium. This can be attributed to the strong hydrogen bonding, facilitating the growth of dense and uniform perovskite films. Besides, GA$^+$ acting as a spacer tends to form a polydisperse domain distribution in quasi-2D perovskite films, while BA$^+$ spacer favors a monodisperse domain distribution. The addition of GA$^+$ also results in the coordination of the amine or imine ($-NH_2$ or $=NH$) groups with lead defects, hence enhancing the performance of these films. This work offers a facile strategy to enhance the morphological and optical properties of perovskites, hence having the potential to accelerate their technological advancement.

4. Experimental Section

Materials: 1,3,5-tris(1-phenyl-1H-benzimidazol-2-yl)benzene (TPBI) and lithium fluoride (LiF) were purchased from Luminescence Technology. CsBr (99.999%), PbBr$_2$ (99.999%), butylammonium bromide (BABr, 99.0%), poly(9,9-dioctylfluorenyl-2,7-diyl)-co-(4,4′-(N-(4-sec-butylphenyl) diphenylamine) (TFB, 99.0%), poly(9-vinylcarbazole) (PVK, 99.999%), and dimethyl sulfoxide (DMSO, 99.8%) were purchased from Sigma-Aldrich. Guanidinium bromide (GABr, 99.0%) was purchased from Xi'an Polymer Light Technology Corp. Chlorobenzene (AR) was acquired from Alfa Aesar. All chemicals were used as received without further purification.

Perovskite Precursor Solutions: PbBr$_2$, CsBr, and BABr were dissolved in DMSO in the ratio of 1:1.2:0.4 (Pe (GA-0)).[16] GABr was introduced in the precursor solution to partially replace BABr of the ratio of 0.1, 0.2, and 0.3, (marked as GA-0.1, GA-0.2, and GA-0.3), respectively. The mixture was stirred at 60 °C overnight and filtered through a 0.22 μm polytetrafluoroethylene membrane before use.

Characterization Methods: XRD patterns were recorded using a Bruker D8 Advance diffractometer with Cu Kα radiation range from 5° to 60° at a scanning rate of 6° min^{-1}. Absorption spectra were measured using a Perkin Elmer Lambda 950 UV–vis-NIR spectrometer. The steady-state PL spectra was obtained by using an Edinburgh FLS920 PL spectrometer with an excitation wavelength of 365 nm. XPS and UPS spectra were acquired using a Thermo Scientific Escalab 250Xi. He (I) ultraviolet radiation source (21.22 eV) from a He discharge lamp was used in the UPS measurements. FTIR spectra were recorded under the attenuated total reflectance (ATR) mode (Spectrum 100, PerkinElmer). The GIWAXS data were obtained at beamline BL14B1 of the Shanghai Synchrotron Radiation Facility (SSRF), China. A monochromatic beam of $\lambda = 0.6887$ Å was used, and the incident angle was 0.1°. The EL spectra of the perovskite LEDs were measured using a Shenzhen Pynect integrated sphere (50 cm in diameter) coupled with a Keithley 2400 sourcemeter. All the device characterization and operational stability tests were carried out on unencapsulated perovskite LEDs at room temperature in an N$_2$-filled glovebox.

Device Fabrication: ITO-coated glass substrates (15 Ω per square) were sonication cleaned with detergent, deionized water, acetone, and isopropyl alcohol for 15 min in each solvent. The dried ITO substrates were treated with oxygen plasma for 15 min to improve the hydrophilicity and work function. The substrates were transferred into a nitrogen glove box for device fabrication. TFB:PVK dissolved in chlorobenzene (4:6 in weight ratio with a concentration of 10 mg ml^{-1}) were spin-coated onto the ITO substrates at a speed of 4000 rpm min^{-1} for 40 s and annealed at 150 °C for 15 min. GABr (1 mg mL^{-1}, 2 mg mL^{-1}, 3 mg mL^{-1} in absolute ethyl alcohol) was spin-coated on top of the TFB:PVK layer at 3000 rpm for 40 s, and then annealed at 110 °C for 5 min. For the perovskite film, the precursor solution was spin-coated at 4000 rpm for 40 s and thermally treated at 80 °C for 10 min. After deposition of the perovskite films, TPBI (40 nm) and LiF/Al electrodes (1 nm/100 nm) were sequentially deposited by thermal evaporation at a base pressure of ≈4 × 10^{-4} Pa. The device emitting area was 4 mm^2.

Statistical Analysis: All representative experimental results presented in the Figures are shown as measured. All measurements were performed with a minimum of three independent replicates and the results are shown as mean ± SD.

Supporting Information

Supporting Information is available from the Wiley Online Library or from the author.

Conflict of Interest

The authors declare no conflict of interest.

Data Availability Statement

The data that support the findings of this study are available from the corresponding author upon reasonable request.

[1] A. Fakharuddin, M. K. Gangishetty, M. Abdi-Jalebi, S.-H. Chin, A. R. bin Mohd Yusoff, D. N. Congreve, W. Tress, F. Deschler, M. Vasilopoulou, H. J. Bolink, *Nat. Electron.* **2022**, *5*, 203.

[2] H. Wang, X. Zhang, Q. Wu, F. Cao, D. Yang, Y. Shang, Z. Ning, W. Zhang, W. Zheng, Y. Yan, S. V. Kershaw, L. Zhang, A. L. Rogach, X. Yang, *Nat. Commun.* **2019**, *10*, 665.

[3] K. Lin, J. Xing, L. N. Quan, F. P. G. de Arquer, X. Gong, J. Lu, L. Xie, W. Zhao, D. Zhang, C. Yan, W. Li, X. Liu, Y. Lu, J. Kirman, E. H. Sargent, Q. Xiong, Z. Wei, *Nature* **2018**, *562*, 245.

[4] M. Liu, Q. Wan, H. Wang, F. Carulli, X. Sun, W. Zheng, L. Kong, Q. Zhang, C. Zhang, Q. Zhang, S. Brovelli, L. Li, *Nat. Photonics* **2021**, *15*, 379.

[5] C. Zhang, S. Wang, X. Li, M. Yuan, L. Turyanska, X. Yang, *Adv. Funct. Mater.* **2020**, *30*, 1910582.

[6] D. Ma, K. Lin, Y. Dong, H. Choubisa, A. H. Proppe, D. Wu, Y.-K. Wang, B. Chen, P. Li, J. Z. Fan, F. Yuan, A. Johnston, Y. Liu, Y. Kang, Z.-H. Lu, Z. Wei, E. H. Sargent, *Nature* **2021**, *599*, 594.

[7] Y. Cao, N. Wang, H. Tian, J. Guo, Y. Wei, H. Chen, Y. Miao, W. Zou, K. Pan, Y. He, H. Cao, Y. Ke, M. Xu, Y. Wang, M. Yang, K. Du, Z. Fu, D. Kong, D. Dai, Y. Jin, G. Li, H. Li, Q. Peng, J. Wang, W. Huang, *Nature* **2018**, *562*, 249.

[8] B. Guo, R. Lai, S. Jiang, L. Zhou, Z. Ren, Y. Lian, P. Li, X. Cao, S. Xing, Y. Wang, W. Li, C. Zou, M. Chen, Z. Hong, C. Li, B. Zhao, D. Di, *Nat. Photonics* **2022**, *16*, 637.

[9] F. Yang, H. Chen, R. Zhang, X. Liu, W. Zhang, J. Zhang, F. Gao, L. Wang, *Adv. Funct. Mater.* **2020**, *30*, 1908760.

[10] X. Liu, W. Xu, S. Bai, Y. Jin, J. Wang, R. H. Friend, F. Gao, *Nat. Mater.* **2021**, *20*, 10.

[11] H. Wang, X. Gong, D. Zhao, Y.-B. Zhao, S. Wang, J. Zhang, L. Kong, B. Wei, R. Quintero-Bermudez, O. Voznyy, Y. Shang, Z. Ning, Y. Yan, E. H. Sargent, X. Yang, *Joule* **2020**, *4*, 1977.

[12] X. Wang, X. Zhang, J. Deng, Z. Chu, Q. Jiang, J. Meng, P. Wang, L. Zhang, Z. Yin, J. You, *Nat. Commun.* **2018**, *9*, 570.

[13] J. Tang, W. Tian, C. Zhao, Q. Sun, C. Zhang, H. Cheng, Y. Shi, S. Jin, *ACS Omega* **2022**, *7*, 10365.

[14] D. Li, Z. Xing, L. Huang, X. Meng, X. Hu, T. Hu, Y. Chen, *Adv. Mater.* **2021**, *33*, 2101823.

[15] Z. Liu, W. Qiu, X. Peng, G. Sun, X. Liu, D. Liu, Z. Li, F. He, C. Shen, Q. Gu, F. Ma, H.-L. Yip, L. Hou, Z. Qi, S.-J. Su, *Adv. Mater.* **2021**, *33*, 2103268.

[16] L. Kong, X. Zhang, Y. Li, H. Wang, Y. Jiang, S. Wang, M. You, C. Zhang, T. Zhang, S. V. Kershaw, W. Zheng, Y. Yang, Q. Lin, M. Yuan, A. L. Rogach, X. Yang, *Nat. Commun.* **2021**, *12*, 1246.

[17] Akriti, S. Z. , Z.-Y. Lin, E. Shi, B. P. Finkenauer, Y. Gao, A. J. Pistone, K. Ma, B. M. Savoie, L. Dou, *Adv. Mater.* **2021**, *33*, 2105183.

[18] N. Li, Y. Jia, Y. Guo, N. Zhao, *Adv. Mater.* **2022**, *34*, 2108102.

[19] L. Lei, D. Seyitliyev, S. Stuard, J. Mendes, Q. Dong, X. Fu, Y.-A. Chen, S. He, X. Yi, L. Zhu, C.-H. Chang, H. Ade, K. Gundogdu, F. So, *Adv. Mater.* **2020**, *32*, 1906571.

[20] Y. Tian, C. Zhou, M. Worku, X. Wang, Y. Ling, H. Gao, Y. Zhou, Y. Miao, J. Guan, B. Ma, *Adv. Mater.* **2018**, *30*, 1707093.

[21] Y.-H. Kim, C. Wolf, Y.-T. Kim, H. Cho, W. Kwon, S. Do, A. Sadhanala, C. G. Park, S.-W. Rhee, S. H. Im, R. H. Friend, T.-W. Lee, *ACS Nano* **2017**, *11*, 6586.

[22] H. Cho, S.-H. Jeong, M.-H. Park, Y.-H. Kim, C. Wolf, C.-L. Lee, J. H. Heo, A. Sadhanala, N. Myoung, S. Yoo, S. H. Im, R. H. Friend, T.-W. Lee, *Science* **2015**, *350*, 1222.

[23] H. Wang, C. C. S. Chan, M. Chu, J. Xie, S. Zhao, X. Guo, Q. Miao, K. S. Wong, K. Yan, J. Xu, *Sol. RRL* **2020**, *4*, 1900578.

[24] J. K. Mishra, N. Yantara, A. Kanwat, T. Furuhashi, S. Ramesh, T. Salim, N. F. Jamaludin, B. Febriansyah, Z. E. Ooi, S. Mhaisalkar, T. C. Sum, K. Hippalgaonkar, N. Mathews, *ACS Appl. Mater. Interfaces* **2022**, *14*, 34238.

[25] H. Xu, Z. Liang, J. Ye, S. Xu, Z. Wang, L. Zhu, X. Chen, Z. Xiao, X. Pan, G. Liu, *Chem. Eng. J.* **2022**, *437*, 135181.

[26] W. Li, A. Thirumurugan, P. T. Barton, Z. Lin, S. Henke, H. H. M. Yeung, M. T. Wharmby, E. G. Bithell, C. J. Howard, A. K. Cheetham, *J. Am. Chem. Soc.* **2014**, *136*, 7801.

[27] G. Wu, R. Liang, Z. Zhang, M. Ge, G. Xing, G. Sun, *Small* **2021**, *17*, 2103514.

[28] Y.-M. Xie, Q. Xue, H.-L. Yip, *Adv. Energy Mater.* **2021**, *11*, 2100784.

[29] W. Zhang, J. Xiong, J. Li, W. A. Daoud, *J. Mater. Chem. A* **2019**, *7*, 9486.

[30] Y. Huang, Y. Li, E. L. Lim, T. Kong, Y. Zhang, J. Song, A. Hagfeldt, D. Bi, *J. Am. Chem. Soc.* **2021**, *143*, 3911.

[31] W. Cha, H. Han, Y. Hong, G. Kim, C. Park, D. Kim, *J. Phys. Chem. C* **2020**, *124*, 4414.

[32] M. Long, T. Zhang, D. Chen, M. Qin, Z. Chen, L. Gong, X. Lu, F. Xie, W. Xie, J. Chen, J. Xu, *ACS Energy Lett.* **2019**, *4*, 1025.

[33] L. Zhang, F. Yuan, J. Xi, B. Jiao, H. Dong, J. Li, Z. Wu, *Adv. Funct. Mater.* **2020**, *30*, 2001834.

[34] A. H. Proppe, R. Quintero-Bermudez, H. Tan, O. Voznyy, S. O. Kelley, E. H. Sargent, *J. Am. Chem. Soc.* **2018**, *140*, 2890.

[35] L. N. Quan, Y. Zhao, F. P. García de Arquer, R. Sabatini, G. Walters, O. Voznyy, R. Comin, Y. Li, J. Z. Fan, H. Tan, J. Pan, M. Yuan, O. M. Bakr, Z. Lu, D. H. Kim, E. H. Sargent, *Nano Lett.* **2017**, *17*, 3701.

[36] M. Yuan, L. N. Quan, R. Comin, G. Walters, R. Sabatini, O. Voznyy, S. Hoogland, Y. Zhao, E. M. Beauregard, P. Kanjanaboos, Z. Lu, D. H. Kim, E. H. Sargent, *Nat. Nanotechnol.* **2016**, *11*, 872.

[37] C. Xiong, Y. Li, S. Wang, Y. Zhou, *J. Mol. Liq.* **2018**, *256*, 183.

[38] M. Rozenberg, G. Shoham, I. Reva, R. Fausto, *Spectrochim. Acta A Mol. Biomol. Spectrosc.* **2003**, *59*, 3253.

[39] Y. Zhou, C. Fuentes-Hernandez, J. Shim, J. Meyer, J. Giordano Anthony, H. Li, P. Winget, T. Papadopoulos, H. Cheun, J. Kim, M. Fenoll, A. Dindar, W. Haske, E. Najafabadi, M. Khan Talha, H. Sojoudi, S. Barlow, S. Graham, J.-L. Brédas, R. Marder Seth, A. Kahn, B. Kippelen, *Science* **2012**, *336*, 327.